Euclid preparation. XXXIV. The effect of linear redshift-space distortions in photometric galaxy clustering and its cross-correlation with cosmic shear

Euclid Collaboration: K. Tanidis[1,2]★, V. F. Cardone[3,4], M. Martinelli[3,4], I. Tutusaus[5,6], S. Camera[7,8,9], N. Aghanim[10], A. Amara[11], S. Andreon[12], N. Auricchio[13], M. Baldi[14,13,15], S. Bardelli[13], E. Branchini[16,17], M. Brescia[18,19], J. Brinchmann[20], V. Capobianco[9], C. Carbone[21], J. Carretero[22,23], S. Casas[24], M. Castellano[3], S. Cavuoti[19,25], A. Cimatti[26], R. Cledassou[27,28]★★, G. Congedo[29], L. Conversi[30,31], Y. Copin[32], L. Corcione[9], F. Courbin[33], H. M. Courtois[34], A. Da Silva[35,36], H. Degaudenzi[37], J. Dinis[36,35], F. Dubath[37], X. Dupac[31], S. Dusini[38], M. Farina[39], S. Farrens[40], S. Ferriol[32], P. Fosalba[41,42], M. Frailis[43], E. Franceschi[13], M. Fumana[21], S. Galeotta[43], B. Garilli[21], W. Gillard[44], B. Gillis[29], C. Giocoli[13,15], A. Grazian[45], F. Grupp[46,47], L. Guzzo[48,12,49], S. V. H. Haugan[50], W. Holmes[51], I. Hook[52], A. Hornstrup[53,54], K. Jahnke[55], B. Joachimi[56], E. Keihanen[57], S. Kermiche[44], A. Kiessling[51], M. Kunz[6], H. Kurki-Suonio[58,59], P. B. Lilje[50], V. Lindholm[58,59], I. Lloro[60], E. Maiorano[13], O. Mansutti[43], O. Marggraf[61], K. Markovic[51], N. Martinet[62], F. Marulli[63,13,15], R. Massey[64], S. Maurogordato[65], E. Medinaceli[13], S. Mei[66], M. Meneghetti[13,15], G. Meylan[33], M. Moresco[63,13], L. Moscardini[63,13,15], E. Munari[43], S.-M. Niemi[67], C. Padilla[22], S. Paltani[37], F. Pasian[43], K. Pedersen[68], W. J. Percival[69,70,71], V. Pettorino[72], S. Pires[40], G. Polenta[73], J. E. Pollack[74,66], M. Poncet[27], L. A. Popa[75], F. Raison[46], A. Renzi[76,38], J. Rhodes[51], G. Riccio[19], E. Romelli[43], M. Roncarelli[13], E. Rossetti[14], R. Saglia[77,46], D. Sapone[78], B. Sartoris[77,43], M. Schirmer[55], P. Schneider[61], A. Secroun[44], G. Seidel[55], S. Serrano[42,41,79], C. Sirignano[76,38], G. Sirri[15], L. Stanco[38], P. Tallada-Crespí[80,23], A. N. Taylor[29], I. Tereno[35,81], R. Toledo-Moreo[82], F. Torradeflot[23,80], E. A. Valentijn[83], L. Valenziano[13,84], T. Vassallo[77,43], A. Veropalumbo[12], Y. Wang[85], J. Weller[77,46], G. Zamorani[13], J. Zoubian[44], E. Zucca[13], A. Biviano[43,86], A. Boucaud[66], E. Bozzo[37], C. Colodro-Conde[87], D. Di Ferdinando[15], R. Farinelli[13], J. Graciá-Carpio[46], S. Marcin[88], N. Mauri[26,15], V. Scottez[89,90], M. Tenti[84], A. Tramacere[37], Y. Akrami[91,92,93,94,95], V. Allevato[19,96], C. Baccigalupi[97,43,98], A. Balaguera-Antolínez[87,99], M. Ballardini[100,101,13], D. Benielli[44], F. Bernardeau[102,103], S. Borgani[43,104,98,86], A. S. Borlaff[105,106], C. Burigana[107,84], R. Cabanac[5], A. Cappi[13,65], C. S. Carvalho[81], G. Castignani[63,13], T. Castro[43,98,86], G. Cañas-Herrera[67,108], K. C. Chambers[109], A. R. Cooray[110], J. Coupon[37], A. Díaz-Sánchez[111], S. Davini[17], S. de la Torre[62], G. De Lucia[43], G. Desprez[112], S. Di Domizio[113], H. Dole[10], J. A. Escartin Vigo[46], S. Escoffier[44], P. G. Ferreira[2], I. Ferrero[50], F. Finelli[13,84], L. Gabarra[76,38], J. García-Bellido[91], E. Gaztanaga[41,42,11], F. Giacomini[15], G. Gozaliasl[58,114], H. Hildebrandt[115], S. Ilić[116,27,5], J. J. E. Kajava[117,118], V. Kansal[119], C. C. Kirkpatrick[57], L. Legrand[6], A. Loureiro[120,95], J. Macias-Perez[121], M. Magliocchetti[39], G. Mainetti[122], R. Maoli[123,3], C. J. A. P. Martins[124,20], S. Matthew[29], L. Maurin[10], R. B. Metcalf[63], M. Migliaccio[125,126], P. Monaco[104,43,98,86], G. Morgante[13], S. Nadathur[11], A. A. Nucita[127,128,129], M. Pöntinen[58], L. Patrizii[15], A. Pezzotta[46], V. Popa[75], D. Potter[130], A. G. Sánchez[46], Z. Sakr[131,5,132], J. A. Schewtschenko[29], A. Schneider[130], M. Sereno[13,15], P. Simon[61], A. Spurio Mancini[133], J. Steinwagner[46], M. Tewes[61], R. Teyssier[134], S. Toft[54,135,136], J. Valiviita[58,59], M. Viel[86,43,97,98], L. Linke[137]

(Affiliations can be found after the references)

November 29, 2023

ABSTRACT

Context. Cosmological surveys planned for the current decade will provide us with unparalleled observations of the distribution of galaxies on cosmic scales, by means of which we can probe the underlying large-scale structure (LSS) of the Universe. This will allow us to test the concordance cosmological model and its extensions. However, precision pushes us to high levels of accuracy in the theoretical modelling of the LSS observables, in order not to introduce biases in the estimation of cosmological parameters. In particular, effects such as redshift-space distortions (RSD) can become relevant in the computation of harmonic-space power spectra even for the clustering of the photometrically selected galaxies, as it has been previously shown in literature studies.

Aims. In this work, we investigate the contribution of linear RSD, as formulated in the Limber approximation by a previous work, in forecast cosmological analyses with the photometric galaxy sample of the *Euclid* survey, in order to assess their impact and quantify the bias on the measurement of cosmological parameters that neglecting such an effect would cause.

Methods. We perform this task by producing mock power spectra for photometric galaxy clustering and weak lensing, as expected to be obtained from the *Euclid* survey. We then use a Markov chain Monte Carlo approach to obtain the posterior distributions of cosmological parameters from such simulated observations.

Results. We find that neglecting the linear RSD leads to significant biases both when using galaxy correlations alone and when these are combined with cosmic shear, in the so-called 3×2pt approach. Such biases can be as large as 5 σ-equivalent when assuming an underlying ΛCDM cosmology. When extending the cosmological model to include the equation-of-state parameters of dark energy, we find that the extension parameters can be shifted by more than 1 σ.

Key words. Cosmology: theory – large-scale structure of the Universe – cosmological parameters

1. Introduction

Within the current decade, several large-scale structure (LSS) surveys are expected to start their operations or to release their first results, and they will provide a significant improvement to available cosmological data sets. Such forthcoming LSS surveys will map the matter distribution in the Universe with exquisite precision. Some of them will be ground-based, such as the Dark Energy Spectroscopic Instrument (DESI, DESI Collaboration: Aghamousa et al. 2016a,b), the Legacy Survey of Space and Time (LSST) at the Vera C. Rubin Observatory (LSST Science Collaboration: Abell et al. 2009; LSST Dark Energy Science Collaboration: Mandelbaum et al. 2018; Ivezić et al. 2019), and the SKA Observatory (SKAO; see, e.g., Abdalla et al. 2015; Santos et al. 2015; Brown et al. 2015; Bull et al. 2015; Camera et al. 2015b; Raccanelli et al. 2015; SKA Cosmology Science Working Group 2020). Others will be space-borne, such as the *Euclid* satellite (Laureijs et al. 2011; Amendola et al. 2013, 2018; Euclid Collaboration: Blanchard et al. 2020), the *Nancy Grace Roman* Space Telescope (Spergel et al. 2015), and the Spectro-Photometer for the History of the Universe, Epoch of Reionization, and Ices Explorer (SPHEREx; see, e.g., Doré et al. 2014, 2018).

All the aforementioned surveys rely on the observation of galaxy positions and shapes, with which one can construct summary statistics customarily referred to in cosmology as galaxy clustering (GC) and weak lensing (WL). This can be done in multiple ways, either using the real-space 2pt correlation function, or the harmonic-space power spectrum as we study here, or even via other statistics like COSEBIs (Schneider et al. 2010), or higher-order statistics (Euclid Collaboration: Ajani et al. 2023). The GC encodes information on the clustering of matter due to the effect of gravity, while the WL on the projected matter distribution thanks to its gravitational lensing effect.

In this work, we focus on *Euclid* and its surveys.[1] *Euclid* is a European Space Agency medium-class space mission whose launch took place on the 1st of July 2023. It will perform photometric and spectroscopic galaxy surveys over an area of ∼ 15000 deg^2 of the extragalactic sky (Laureijs et al. 2011), thanks to the near-infrared instrument (Costille et al. 2018) and the visible imager (Cropper et al. 2018), which will be carried on board. The photometric survey will measure the positions and shapes of over a billion galaxies, enabling the analysis of photometric GC (GCph) and WL. As photometric measurements will provide relatively uncertain redshift measurements (compared to spectroscopic observations), the analyses of these observables will be performed via a tomographic approach, binning galaxies in redshift slices and considering the projected two-dimensional data sets. The precise radial measurements of the spectroscopic survey will instead allow us to perform a spectroscopic GC (GCsp) analysis, that is a galaxy clustering analysis in three dimensions.

In Euclid Collaboration: Blanchard et al. (2020, 'Euclid preparation: VII', hereafter EP:VII), the constraints expected from *Euclid* have been forecast, both for the individual GCsp, GCph, and WL probes and for their full combination. In obtaining these results, EP:VII used several assumptions to simplify the theoretical computation of observables: the Limber approximation was used for all the photometric observables, and for GCph it was assumed that the only non-negligible contribution to the galaxy positions correlation function comes from the anisotropies in the density field. It is known, however, that several other effects contribute to GCph, including lensing magnification, velocity, and relativistic effects (Yoo 2010; Challinor & Lewis 2011; Bonvin & Durrer 2011).

Such various contributions can be significant at very large scales, which we define as those corresponding to a wavenumber smaller than that at which peaks the matter power spectrum at the matter-radiation equality scale. Such scales are effectively within reach of wide surveys such as *Euclid*, and it has been shown that neglecting them could lead to inaccurate results, with the cosmology recovered through parameter estimation pipelines significantly biased with respect to the true underlying cosmology (Camera et al. 2015a; Tanidis & Camera 2019; Tanidis et al. 2019; Martinelli et al. 2022; Lepori et al. 2022).

In this work, we focus on one of the most important effects, namely redshift-space distortion (RSD), and we aim at specifically quantifying its impact on the expected results of the *Euclid* wide survey. The effect of the linear RSD on the angular clustering is not new and has been thoroughly studied in the literature the past years (Scharf et al. 1994; Heavens & Taylor 1995; Padmanabhan et al. 2007; Blake et al. 2007; Nock et al. 2010; Crocce et al. 2011; Balaguera-Antolínez et al. 2018; Tanidis & Camera 2019). They have also been included in the Dark Energy Survey (DES, DES Collaboration: Abbott et al. 2005) 3×2pt data analysis for Y3 in the configuration space (Abbott et al. 2022), though they were initially neglected in the Y1 analysis for the galaxy clustering in the configuration and harmonic space (Elvin-Poole et al. 2018; Andrade-Oliveira et al. 2021). Here, we apply the approach of Tanidis & Camera (2019), where the linear RSD contribution to GC harmonic-space power spectra is obtained within the Limber approximation, and examine it in the *Euclid* wide survey. This allows us to perform the computation of the theoretical prediction at a reasonable speed, to use it for parameter estimation. Moreover, in this paper we shall focus on GCph only, not discussing GCsp at all. Therefore, hereafter we shall always refer to the GCph probe simply as GC.

The paper is organised as follows. The equations used to compute the theoretical predictions for the observables of interest are reviewed in Sect. 2, where we also outline how RSD enter in the calculations. In Sect. 2.4 we summarise the results of the Flagship simulation galaxy catalogue. Our analysis method is shown in Sect. 3 and the results obtained in Sect. 4. We finally summarise our conclusions in Sect. 5.

⋆ e-mail: konstantinos.tanidis@physics.ox.ac.uk
⋆⋆ Deceased
[1] http://www.euclid-ec.org/.

2. Photometric observables in *Euclid*

2.1. Harmonic-space power spectra

The harmonic-space power spectrum $C_\ell^{AB}(z_i, z_j)$ between an observable A in the redshift bin i and an observable B in the redshift bin j is defined as:

$$\left\langle A_{i,\ell m} B_{j,\ell'm'}^* \right\rangle = C_\ell^{AB}(z_i, z_j)\, \delta_{\ell\ell'}^{\rm K}\, \delta_{mm'}^{\rm K}\ , \tag{1}$$

where $X_{\ell m}$ are the coefficients of the harmonic expansion of observable X, and $\delta^{\rm K}$ denotes the Kronecker symbol. Here, letters A and B stand for the observables of interest: galaxy number counts fluctuations, Δ, or galaxy ellipticities, ϵ. Both fields are discussed in more detail in Sect. 2.2 and Sect. 2.3, respectively.

Within the Limber approximation (Kaiser 1992), valid at $\ell \gg 1$ and for broad redshift kernels, the harmonic-space (also, angular) power spectrum between two observables A and B is

$$C_{ij}^{AB}(\ell) = \int \frac{{\rm d}r}{r^2}\, W_i^A(\ell, r)\, W_j^B(\ell, r)\, P_{\delta\delta}\left(k = \frac{\ell + 1/2}{r}, r\right)\ , \tag{2}$$

where $P_{\delta\delta}$ is the (non-linear) matter power spectrum, $k = |\boldsymbol{k}|$ the wave number, which is the Fourier mode related to the comoving separation between pairs of galaxies in configuration space, and $r(z)$ is the radial comoving distance to redshift z for a flat cosmology. The generic redshift-binned kernel $W_i^A(\ell, r)$ takes different forms depending on the target observables as we will see in Sect. 2.2 and Sect. 2.3. Note that we use the notation $C_{ij}^{AB}(\ell)$ as in EP:VII, as opposed to $C_\ell^{AB}(z_i, z_j)$ of Eq. (1), to denote the fact that we refer to the Limber-approximated power spectrum.

2.2. Linear RSD in GCph

In GC, galaxies are biased tracers of the underlying matter field (Kaiser 1987). At sufficiently large scales, the bias can be considered dependent only on redshift and not on scale (Abbott et al. 2018). On the other hand, when adding non-linear scales the galaxy bias becomes non-local and a specific treatment should account for this effect (Sánchez et al. 2016; Desjacques et al. 2018). On top of this, RSD are additional observational effects due to the peculiar velocities of galaxies (Kaiser 1987; Szalay et al. 1998). These are customarily split into linear RSD (a.k.a. the Kaiser effect) and non-linear RSD (a.k.a. the Fingers-of-God, 'FoG' hereafter). The former is responsible for the squashing of the galaxy two-point correlation function on large scales in the direction perpendicular to the line of sight, while the latter enhances the clustering amplitude along the line-of-sight direction on small scales. In the current analysis we consider a simple model, assuming that the galaxy bias is linear and scale-independent, and only accounting for linear RSD. The modelling of the non-linear galaxy bias and the FoG as well as their effects in the photometric observables for *Euclid* is left for future work. The kernel of Eq. (2) in the case of the GC including up to linear RSD in the Limber approximation (for details, see Tanidis & Camera 2019) takes the form

$$W_i^{\Delta}(\ell, r) = W_i^{\rm den}(r) + W_i^{\rm RSD}(\ell, r)\ , \tag{3}$$

with the first term being due to fluctuations in the density field,

$$W_i^{\rm den}(r) = n_i(r)\, b_i(r)\ , \tag{4}$$

with $n_i(r)\,{\rm d}r$ the galaxy probability density in bin i between comoving distance r and $r + {\rm d}r$, and b_i being the corresponding

linear galaxy bias, computed at $r \equiv r(z)$. This, we treat as a constant within the redshift bin, and its actual amplitude is a nuisance parameter, which we marginalise over in our analysis. For the fiducial galaxy bias values in each bin (see Table 2) we use the fiducial model of Euclid Collaboration: Pocino et al. (2021, 'Euclid Colaboration: XII', hereafter EP:XII) where the authors have considered a magnitude cut at $I_{\rm E} = 24.5$ for the *Euclid* imager that will observe through an optical broad band. For the galaxy distributions $n_i(r)$, we use the outcome of the Flagship galaxy simulation of the Euclid Consortium, for which we provide details in Sect. 2.4.

The second term in Eq. (3) is the RSD contribution (Tanidis & Camera 2019),

$$W_i^{\rm RSD}(\ell, r) = \sum_{n=-1}^{1} L_n(\ell)\, n_i\left(\frac{2\ell + 1 + 4n}{2\ell + 1}\, r\right) f\left(\frac{2\ell + 1 + 4n}{2\ell + 1}\, r\right)\ , \tag{5}$$

with

$$L_0(\ell) = \frac{2\ell^2 + 2\ell - 1}{(2\ell - 1)(2\ell + 3)}\ , \tag{6}$$

$$L_{-1}(\ell) = -\frac{\ell(\ell - 1)}{(2\ell - 1)\sqrt{(2\ell - 3)(2\ell + 1)}}\ , \tag{7}$$

$$L_{+1}(\ell) = -\frac{(\ell + 1)(\ell + 2)}{(2\ell + 3)\sqrt{(2\ell + 1)(2\ell + 5)}}\ . \tag{8}$$

In Eq. (5), $f := -(1 + z)\,{\rm d}\ln D/{\rm d}z$ is the growth rate, with D being the linear growth factor. In the top panel of Fig. 1, we quantify the signal loss when the linear RSD are not included in the photometric GC harmonic-space power spectrum. In particular, we see that RSD are important at large scales, approximately for $\ell \lesssim 100$. Additionally, the contribution to the total signal increases with redshift for a given redshift bin width. For example, RSD contribute to the total signal from 2–3% at low redshift (purple, solid curve, bin pair 1–1) and gradually increase with increasing redshift (yellow, dash-dotted curve, bin pair 6–6) up to $\sim 40\%$ at the lowest available multipoles. However, we should note that this is not true for the highest redshift bin (blue, dotted curve, bin pair 13–13). Indeed, this bin contributes less to the full signal than , e.g., the bin pairs 10–10 and 6–6 do. It has been shown in Tanidis et al. (2019) that the linear RSD effect is gradually diluted when the width of the redshift bin increases. This is particularly the case for the highest redshift bins due to the large photometric uncertainties at high redshifts.

Another important correction to the galaxy density field is the magnification bias. As in this work we want to quantify the impact of linear RSD alone on *Euclid* photometric observables, we neglect the magnification effect in our analysis. However, the impact of this effect has been thoroughly studied in Lepori et al. (2022) (in that study the linear RSD were neglected), and its inclusion is found to be crucial to avoid biases on the cosmological parameter estimation for *Euclid*. Similar studies on this effect have also been conducted for other future experiments (Tanidis et al. 2019).

Apart from these, there are also local and integrated and contributions to the signal that are measurable at ultra-large scales, such as the Doppler terms, the Sachs-Wolfe and the integrated Sachs-Wolfe effects, and the time delay. We neglect these contributions in our analysis, since for $\ell \gg 1$, where the Limber approximation holds, their effect is negligible (Yoo 2010; Challinor & Lewis 2011; Bonvin & Durrer 2011; Martinelli et al. 2022).
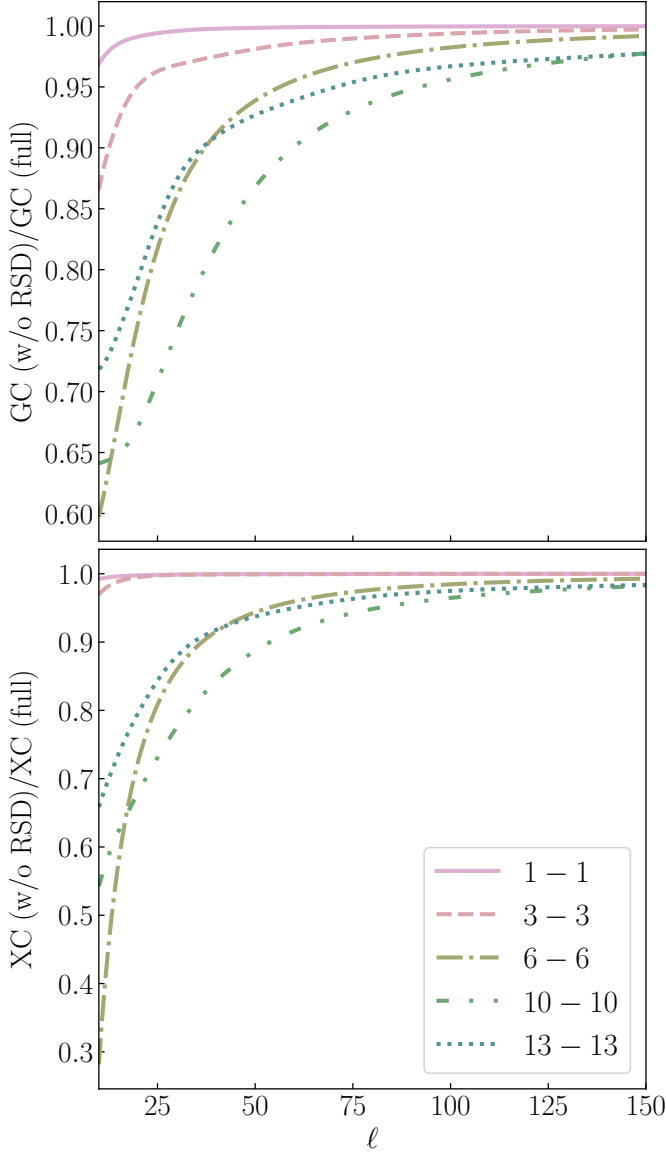
Fig. 1. Ratio of the harmonic-space power spectrum for the density fluctuations alone, with respect to that including RSD, for some tomographic auto-bin correlations ($i = j$). *Top:* GC, *Bottom:* XC.

2.3. Cosmic shear

The LSS of the Universe deflects the paths of photons emitted by distant sources and consequently distorts the source images. This distortion is decomposed into the convergence, κ, and shear, γ, which respectively correspond to size magnification and shape distortion of the images and are linearly related. Both signals contain useful cosmological information, but the former is more impossible to extract because it requires knowledge of the original source sizes (Heavens et al. 2013; Alsing et al. 2015). For this reason, shear is the usual focus of weak lensing surveys of the LSS.

The harmonic-space power spectrum of the shear field is a probe of the growth of structures and the cosmological expansion. Apart from the cosmic shear, the correlation of the galaxy shapes also receives a contribution from intrinsic alignments (hereafter IA), which in the context of cosmological weak lensing studies is regarded as a systematic effect. This accounts for the fact that, apart from the random orientations of galaxies

which would ideally make the ellipticity an unbiased estimator of the shear field, there are also IA of the galaxies due to the tidal interactions during galaxy formation, as well as astrophysical effects, contaminating the weak lensing analysis (Joachimi et al. 2015).

For the WL sample, the kernel of observed ellipticity power spectrum including cosmic shear γ and IA, reads

$$W_i^\epsilon(\ell, r) = W_i^\gamma(\ell, r) + W_i^{IA}(r) . \tag{9}$$

The shear contribution is

$$W_i^\gamma(\ell, r) = \frac{3 L_\gamma(\ell) \, \Omega_{m,0} \, H_0^2}{2c^2} [1 + z(r)] \, r \, q_i(r) , \tag{10}$$

where c is the vacuum speed of light, $q_i(r)$ is the so-called lensing efficiency for a flat Universe,

$$q_i(r) = \int_r^\infty dr' \frac{r' - r}{r'} \, n_i(r') , \tag{11}$$

and the ℓ-dependent factor is given by

$$L_\gamma(\ell) = \sqrt{\frac{(\ell + 2)!}{(\ell - 2)!} \left(\frac{2}{2\,\ell + 1} \right)^2} . \tag{12}$$

For WL, too, we use the $n_i(r)$ obtained from the Flagship simulation of Sect. 2.4. Since in our analysis we restrict ourselves to multipoles where the Limber approximation applies ($\ell \gg 1$), this factor can be considered as $L_\gamma(\ell) \approx 1$.

The IA contribution can instead be modelled as in EP:VII, namely

$$W_i^{IA}(r) = -\mathcal{A}_{IA} \, C_{IA} \, \Omega_{m,0} \frac{\mathcal{F}_{IA}[z(r)]}{D[z(r)]} \, n_i(r) , \tag{13}$$

where

$$\mathcal{F}_{IA}(z) = (1 + z)^{\eta_{IA}} \left[\frac{\langle L \rangle(z)}{L_*(z)} \right]^{\beta_{IA}} . \tag{14}$$

The amplitude and shape of the IA signal is captured by the nuisance parameters $\mathcal{A}_{IA}, \beta_{IA}, \eta_{IA}$ (see Table 2 for their fiducial values), with C_{IA} kept fixed at the value 0.0134, since it is degenerate with $\mathcal{A}_{IA}$. The terms $\langle L \rangle(z)$ and $L_*(z)$ denote the mean and the characteristic luminosity of the source galaxies with respect to redshift.[2] Note that we neglect other sources of systematic effects for the WL probe such as the shear bias and the photometric redshift uncertainties (that in principle are also present for the tomographic bins in photometric GC).

In the bottom panel of Fig. 1 we show the signal loss if we neglect the linear RSD contribution in the cross power spectrum between GC and WL (hereafter XC). The picture is very similar compared to the one presented for the GC (top panel of Fig. 1). The main difference is that the RSD contribution to the total signal is less than $\sim 1\%$ at the lowest redshift (bin pair 1–1), reaching at the largest scales a maximum of up to $\sim 70\%$ in bin pair 6–6.

It is worth mentioning that for some bin cases the signal lost by neglecting RSD with respect to the total signal in XC is more than the GC, which indeed seems to be counter-intuitive since the RSD is an additional term in the GC kernel Eq. (3). Although it is true that the RSD kernel given by Eq. (5) appears twice in Eq. (2) for all bin correlations due to Eq. (3) and only once in the

---

[2] We refer the reader to EP:VII for more details concerning the IA modelling.
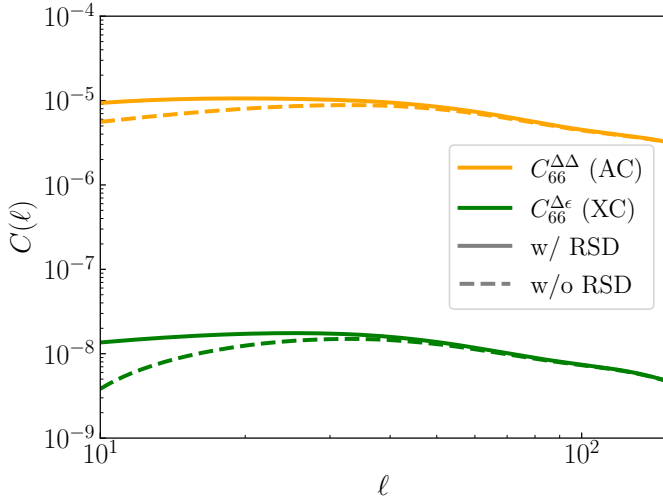
Fig. 2. The GC (orange) and the XC (green) spectrum for the bin correlation 6–6. Dashed lines correspond for spectra w/o RSD while with solid are w/ RSD, respectively.

XC, the GC spectra have more power than the XC ones as it can be seen in Fig. 2. The WL kernel of Eq. (9) also appears once in the XC and is the one that is lowering the signal. For this reason it is possible for the XC spectra to be numerically more affected in the cases where the RSD signal is more important, as is in the bin correlations 6–6 and 10–10.

2.4. The Euclid Flagship simulation

In order to create realistic mock data vectors for our analysis, we use the simulated results from the Flagship galaxy simulation of the Euclid Consortium (Euclid Consortium, in preparation). The galaxy catalogue was produced using the *N*-body Flagship dark matter simulation (Potter et al. 2017) with a ΛCDM fiducial cosmology given by the total matter abundance, $\Omega_{m,0} = 0.319$; the baryon abundance, $\Omega_{b,0} = 0.049$; the r.m.s. variance of the linear matter fluctuations at $z = 0$ in spheres of radius $8\,h^{-1}$ Mpc, $\sigma_8 = 0.830$; the spectral index of the primordial curvature power spectrum, $n_s = 0.96$; and the dimensionless Hubble constant, $h \equiv H_0/(100\,\mathrm{km\,s^{-1}\,Mpc^{-1}}) = 0.67$. The *N*-body simulation ran a box of $3.78\,h^{-1}$ Gpc with a particle mass of $2.398 \times 10^9\,h^{-1}\,M_\odot$.

The dark matter haloes were identified using ROCKSTAR (Behroozi et al. 2013) down to masses of $2.4 \times 10^{10}\,h^{-1}\,M_\odot$ (corresponding to ten particles per halo). Then, the galaxies were assigned to the haloes using the halo occupation distribution and the halo abundance matching methods, following the recipe presented in Carretero et al. (2015). Several observational constraints were used to calibrate the galaxy mocks including the luminosity function (Blanton et al. 2003; Blanton et al. 2005) applied for the faint galaxies, the measurements of galaxy clustering as a function of colour and luminosity (Zehavi et al. 2011), as well as the colour-magnitude diagram from Blanton et al. (2005). The final galaxy catalogue contains close to 3.4 billion galaxies over 5000 deg^2 and extends up to redshift 2.3.

In this work we follow the analysis of EP:XII, where an optimisation of the galaxy sample for photometric GC analyses was performed using the Flagship simulation. The authors in EP:XII generated photometric redshift estimates with the directional neighbourhood fitting training-based algorithm (De Vicente et al. 2016) for all galaxies within a patch of 400 deg^2 of the Flagship simulation up to a magnitude limit of 25 in the
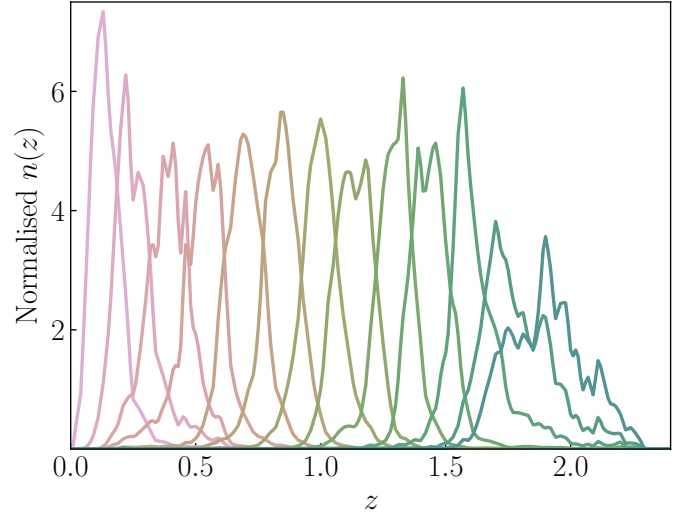

Fig. 3. The normalised number densities of the 13 tomographic equi-spaced bins with redshift as from the *Euclid* Flagship simulation (EP:XII).

Table 1. Fiducial values of cosmological parameters.

$\Omega_{m,0}$	$\Omega_{b,0}$	h	σ_8	n_s	w_0	w_a
0.320	0.050	0.67	0.816	0.96	−1.0	0.0

VIS band. Here, we consider the fiducial sample from EP:XII. This corresponds to a training of the algorithm with an incomplete spectroscopic training sample, to mimic the lack of spectroscopic information at very faint magnitudes, and optimistic magnitude limits for all photometric bands. There is an additional selection of objects with magnitudes brighter than 24.5 in the VIS band. By using the directional neighbourhood fitting algorithm, two different estimates for the photometric redshift are provided for each object. One is the average of the redshifts from the neighbourhood, that we denote z_{mean}. The second estimate is a Monte Carlo draw from the nearest neighbour and that we denote z_{mc}. We refer the reader to EP:XII and De Vicente et al. (2016) for the similarities and differences between these two estimates. The final sample is then composed of 13 tomographic equispaced bins in z_{mean} up to $z = 2$, that is, 13 bins with constant redshift width in z_{mean} and therefore different width in z_{mc}. The normalised number densities of these bins as a function of redshift are shown in Fig. 3. In addition to the galaxy distributions, we also consider the linear galaxy biases for each one of these distributions, which are provided in EP:XII.

3. Synthetic data and analysis methodology

In order to quantify the impact of linear RSD on *Euclid*'s photometric observables, we need to create mock data to compare against our theoretical predictions. For such a purpose, we compute the power spectra for GC, WL, and XC following Eq. (2) in a fiducial cosmology. We choose this to be the same of EP:VII, namely a flat ΛCDM model with one massive and two massless neutrinos fixed to $\sum m_\nu = 0.06$eV. The fiducial values for the parameters are shown in Table 1 and Table 2.

We model the matter power spectrum, $P_{\delta\delta}$, on non-linear small scales using `halofit` (Smith et al. 2003), including corrections for both dark energy (Takahashi et al. 2012) and massive neutrinos (Bird et al. 2012) as in EP:VII. Using these as-

Table 2. Fiducial values of nuisance parameters.

b_1	b_2	b_3	b_4	b_5	b_6	b_7	b_8	b_9	b_{10}	b_{11}	b_{12}	b_{13}	$\mathcal{A}_{\mathrm{IA}}$	β_{IA}	η_{IA}
1.025	1.037	1.066	1.110	1.198	1.293	1.429	1.559	1.758	1.947	2.217	2.537	2.738	1.72	2.17	−0.41

Note: The linear galaxy bias parameter per redshift bin i for GC is denoted with b_i and the WL parameters for the whole redshift range with $\mathcal{A}_{\mathrm{IA}}$, β_{IA}, and η_{IA} (for the resources of the IA modelling, see again EP:VII.). The centres of the redshift bins are the following: $\bar{z}_1 = 0.14$, $\bar{z}_2 = 0.26$, $\bar{z}_3 = 0.39$, $\bar{z}_4 = 0.53$, $\bar{z}_5 = 0.69$, $\bar{z}_6 = 0.84$, $\bar{z}_7 = 1.0$, $\bar{z}_8 = 1.14$, $\bar{z}_9 = 1.3$, $\bar{z}_{10} = 1.44$, $\bar{z}_{11} = 1.62$, $\bar{z}_{12} = 1.78$ and $\bar{z}_{13} = 1.72$.

sumptions, we can compute the harmonic-space power spectra of Eq. (2) for photometric GC, WL, and XC. These will represent our synthetic data set, against which we can compare theoretical predictions from different models to constrain model parameters. In order to do so, we obtain the χ^2 for any set of parameters $\boldsymbol{\theta}$ including cosmological and nuisance, and assume the Gaussian likelihood

$$\chi^2(\boldsymbol{\theta}) = [\boldsymbol{d} - \boldsymbol{t}(\boldsymbol{\theta})]^{\mathsf{T}} \, \mathsf{C}^{-1} \, [\boldsymbol{d} - \boldsymbol{t}(\boldsymbol{\theta})] \ . \tag{15}$$

Note that the data vector $\boldsymbol{d}$, the vector of theoretical predictions $\boldsymbol{t}(\boldsymbol{\theta})$, and the covariance matrix C (which is assumed to be constant and independent of the cosmological parameters), have all been stacked along the i, j, and ℓ indices.

The covariance matrix of the data, C, is the flattened version of the fourth-order Gaussian covariance (as in EP:VII), namely,

$$\mathrm{Cov}\left[C_{ij}^{AB}(\ell), C_{mn}^{A'B'}(\ell')\right] = \frac{\widetilde{C}_{im}^{AA'}(\ell)\,\widetilde{C}_{jn}^{BB'}(\ell) + \widetilde{C}_{in}^{AB'}(\ell)\,\widetilde{C}_{jm}^{BA'}(\ell)}{(2\ell+1)\,\Delta\ell\,f_{\mathrm{sky}}}\,\delta_{\ell\ell'}^{\mathrm{K}} \ , \tag{16}$$

with $\widetilde{C}_{ij}^{AB}(\ell) = C_{ij}^{AB}(\ell) + N_{ij}^{AB}(\ell)$, and $N_{ij}^{AB}(\ell)$ being the noise contribution to the measurement, and $f_{\mathrm{sky}} = 0.3636$ is the sky fraction observed by *Euclid*. Finally, we use

$$N_{ij}^{\Delta\Delta}(\ell) = \frac{1}{\bar{n}_i}\,\delta_{ij}^{\mathrm{K}} \ , \tag{17}$$

$$N_{ij}^{\epsilon\epsilon}(\ell) = \frac{\sigma_\epsilon^2}{\bar{n}_i}\,\delta_{ij}^{\mathrm{K}} \ , \tag{18}$$

$$N_{ij}^{\Delta\epsilon}(\ell) = 0 \ , \tag{19}$$

with $\bar{n}_i$ being the number density of galaxies per steradian in each tomographic bin and σ_ϵ^2 the intrinsic ellipticity variance, which we assume to be $\sigma_\epsilon = 0.3$ (as in EP:VII).

We bin our data in multipoles considering $N_\ell = 20$ logspaced multipole bins in the range $\{\ell_{\mathrm{min}}, \ell_{\mathrm{max}}\}$, with $\Delta\ell$ the width of each bin. We consider the lowest multipole to be $\ell_{\mathrm{min}} = 10$ and consider an optimistic and a pessimistic scenario for the maximum multipole cut ℓ_{max} (see EP:VII), with

– Optimistic | pessimistic GC: 3000 | 750,
– Optimistic | pessimistic WL: 5000 | 1500.

For XC, we conservatively consider the smallest ℓ_{max} (corresponding to the GC values).

At this point, it is important to note that the assumptions we adopt from EP:VII for the purposes of this work in our modelling, are not expected to have a strong impact on the results. For example, an increase in σ_ϵ would have an effect on the WL part but not on the GC and XC. Then, a decrease of $\bar{n}_i$ would increase the shot noise, but the GC part of the analysis, which is the one we are most interested in, with the linear RSD scales, should not be shot-noise dominated. Therefore, the 3×2pt contours would increase through the WL contribution without changing our conclusions on RSD.

With this approach, we now only need one extra ingredient to obtain the χ^2 of Eq. (15), which is the theory vector $\boldsymbol{t}(\boldsymbol{\theta})$. We choose to focus on two models to be constrained with our mock data, which we refer to as ΛCDM and $w_0 w_a$CDM flat cosmologies following the same modelling as in EP:VII. The former has 5 free cosmological parameters which are: $\Omega_{\mathrm{m},0}$, $\Omega_{\mathrm{b},0}$, h, σ_8, and n_{s}. The latter also includes the equation-of-state parameters of dark energy, w_0 and w_a, which come from the CPL parameterisation (Chevallier & Polarski 2001; Linder 2003),

$$w(z) = w_0 + w_a \frac{z}{1+z} \ . \tag{20}$$

As nuisance parameters, both models feature: for GC, linear galaxy bias amplitudes b_i (see Sect. 2.2); and for WL, IA modelling parameters $\mathcal{A}_{\mathrm{IA}}$, β_{IA}, and η_{IA} (see Sect. 2.3).

4. Results

In this section, we use the method presented in Sect. 3 to investigate the impact of the RSD contribution, modelled as in Sect. 2.2, on the final cosmological constraints. We explore the parameter space with a Markov chain Monte Carlo (MCMC) approach using `emcee` (Foreman-Mackey et al. 2013), and we obtain from `CAMB` (Lewis et al. 2000; Howlett et al. 2012) all the quantities needed to compute the theoretical predictions following Eq. (2) in a modified version of the code `CosmoSIS` (Zuntz et al. 2015). We adopt improper (flat) priors for all the parameters in Table 1 and Table 2.

4.1. Validation

Before we proceed with setting up the realistic and computationally expensive MCMC chains for all the different cosmologies and scenarios, we first run a single case with MCMC and compare it to a Fisher matrix forecast (see EP:VII, for details about Fisher forecasts and their derivatives accuracy) in order to validate the pipeline. In brief, entries of the Fisher matrix are constructed as

$$F_{\alpha\beta} = \frac{\partial \boldsymbol{t}^{\mathsf{T}}}{\partial \theta_\alpha}\,\mathsf{C}^{-1}\,\frac{\partial \boldsymbol{t}}{\partial \theta_\beta} \ , \tag{21}$$

where $\{\theta_\alpha\}$ are the elements of the parameter vector $\boldsymbol{\theta}$ (see Sect. 3).

The Fisher forecasts, whose computation is usually faster than any Bayesian sampler, have been used in order to investigate the likelihood curvature of the parameter hyperspace near its peak. In cases where the posterior is very well described by a Gaussian, the Fisher forecasts are particularly accurate, and the smaller the uncertainties on the parameters are, the closer we are to the peak of the posterior where the Gaussian approximation holds. This applies to forthcoming LSS experiments like *Euclid*, which will provide us with an unprecedented large number of sources that will minimise the resulting errors. As expected, the precision will increase even further when we consider all

the available signal. Therefore, we perform a Fisher forecast on the combination of GC, WL, and XC, which we altogether label 3×2pt. We showcase this by considering a $w_0 w_a$CDM cosmological model and an optimistic scale cut, in order to investigate the potential Gaussianity of the posterior in an extended cosmology model with two extra parameters, $\{w_0, w_a\}$. In Eq. (21) we calculate the theory vector $\boldsymbol{t}$ for the fiducial cosmology model and the covariance matrix C following Sect. 3. We also include linear RSD as described in Sect. 2.2. With the same assumptions, we repeat the analysis with an MCMC approach, exploring the posterior and then finding the minimum χ^2 over the parameter space $\boldsymbol{\theta}$.

The comparison between the MCMC and Fisher approaches is shown in the top panel of Fig. 4, where the 68% and 95% credibility levels (C.L.) on cosmological parameters are presented, after the bias and IA parameters have been marginalised over.[3]. The filled green contours correspond to the MCMC and the empty orange contours to the Fisher forecast, respectively. The agreement between the two is remarkable, highlighting the Gaussianity of the posterior, with almost perfectly overlapping constraints and all the directions and widths of the Fisher ellipses recovered by the MCMC. In addition, the fiducial cosmology model values are presented with dotted, black lines, located well within the 68% C.L. contours.

4.2. The contribution of RSD to constraining power

With our MCMC pipeline validated, we now investigate how the additional information encoded in RSD affects the constraining power on the model parameters. For this, we consider GC alone, and not the total 3×2pt since, as shown in Sect. 2.2, RSD is a correction to the GC signal alone and therefore a change in its constraining power would be easier to appreciate.[4] that the RSD also impacts the XC part of the 3×2pt as well, since the latter contains all the combinations of GC, WL, and XC. However, we do not perform the constraining power test due to the RSD in the 3×2pt, since the WL contribution which is not affected by RSD would make the RSD impact less evident. We again focus on the $w_0 w_a$CDM model and the pessimistic scale cut. This is reasonable, given that RSD mostly contributes on scales $\ell < 100$ (see Fig. 1), and therefore a higher ℓ_{max} cut would not affect the constraining power for this test.

In particular, we want to compare the following two models. For the first model, we construct the synthetic data set and covariance matrix for the photometric GC spectra including RSD (GC w/ RSD), and we fit it against the predictions of the $w_0 w_a$CDM model, including RSD. The results of this analysis are shown by the orange contours in the bottom panel of Fig. 4. For the second model, we do exactly the same, but now neither the synthetic data along with the covariance matrix nor the theory model includes the RSD correction (GC w/o RSD); this corresponds to the green contours again in the bottom panel of Fig. 4.

It is clear that the constraints of both models agree very well, indicating that the RSD correction in our modelling does not add significant information on the projected cosmological parameters. This means that despite the fact that the RSD account for up to 40% of the signal for some redshift bins on the largest scales (see again top panel of Fig. 1), the cosmo-

logical information does not come from the large scales since those are cosmic-variance dominated but gradually including smaller scales, where the RSD signal contribution becomes progressively less important.

4.3. Ignoring RSD

Regardless of the absence of additional constraining power on cosmological parameters encoded in linear RSD, we proceed with the investigation of the effect of neglecting RSD in our modelling. Such an investigation was performed with an MCMC analysis in Tanidis & Camera (2019), assuming a *Euclid*-like survey of intermediate width Gaussian bins (with photometric redshift scatter $0.05(1 + z)$), finding that it is crucial to include RSD in the theoretical predictions in order not to bias the cosmological parameters. This outcome of the importance of RSD in the modelling was in agreement with the decision of previous literature works to include them in their analyses (see again the references in Sect. 1). Following the same approach, we create mock data vector and covariance for the *Euclid* survey, with the same specifications as in EP:VII, including the RSD contribution (Sect. 2.2). The data are then analysed assuming an incorrect model, where the RSD contribution is absent. The impact of such an approximation on the accuracy of the final constraints depends on the amplitude of the RSD signal, but also on the details of the experimental noise. For such a reason, we extend the investigation of Tanidis & Camera (2019) which was performed only for GC in a ΛCDM model and in the linear regime [5] for the density field, to more realistic settings. That is, to still consider the linear RSD, but now in the non-linear regime of the density field. In addition, we exploit photometric redshift bins from the Flagship simulation, including massive neutrinos in the analysis, and checking the effect also on the $w_0 w_a$CDM model. Finally, we perform the analysis both for GC alone and for the full 3×2pt, using the pessimistic and optimistic multipole cuts for both cases.

Finally, to have a better insight of the degeneracies that are present in the incorrect modelling, we recast all the final constraints on $\Omega_{m,0}$ and σ_8 in the derived parameter $S_8 = \sigma_8 \sqrt{\Omega_{m,0}/0.3}$. This parameter is particularly informative about the degenerate direction between $\Omega_{m,0}$ and σ_8 in the weak lensing measurements that are included in the 3×2pt. However, for the sake of completeness we calculate it for the GC only as well.

4.3.1. Biased parameter constraints in the photometric GC

We start by obtaining constraints for both the correct (den+RSD) and incorrect models (den-only), using photometric GC alone, both assuming ΛCDM and its extension $w_0 w_a$CDM. To assess the bias on the parameters of interest if an incorrect model is assumed, we use the relative bias which is valid for deterministic quantities assuming no stochasticity (e.g. a noiseless data vector like we consider here),

$$B_\theta = \frac{|\theta^* - \theta^{fid}|}{\sigma_\theta} , \qquad (22)$$

with θ^* being the mean estimated value on the marginalised posterior of the parameter θ, σ_θ the corresponding 68% C.L., and θ^{fid} the input fiducial value. It is defined as the offset we get from

---

[3] Note that 68% and 95% C.L. correspond exactly to 1 and 2 standard deviations in the Gaussian approximation of the Fisher matrix after marginalising over the rest of the parameters

[4] We should mention at this point

[5] In Tanidis & Camera (2019) only the linear matter power spectrum was used and ℓ_{max} was defined by $k_{max} \chi(\bar{z})$ with $k_{max} \simeq 0.25 \, h \, \mathrm{Mpc}^{-1}$ and $\bar{z}$ the mean redshift of the bin.
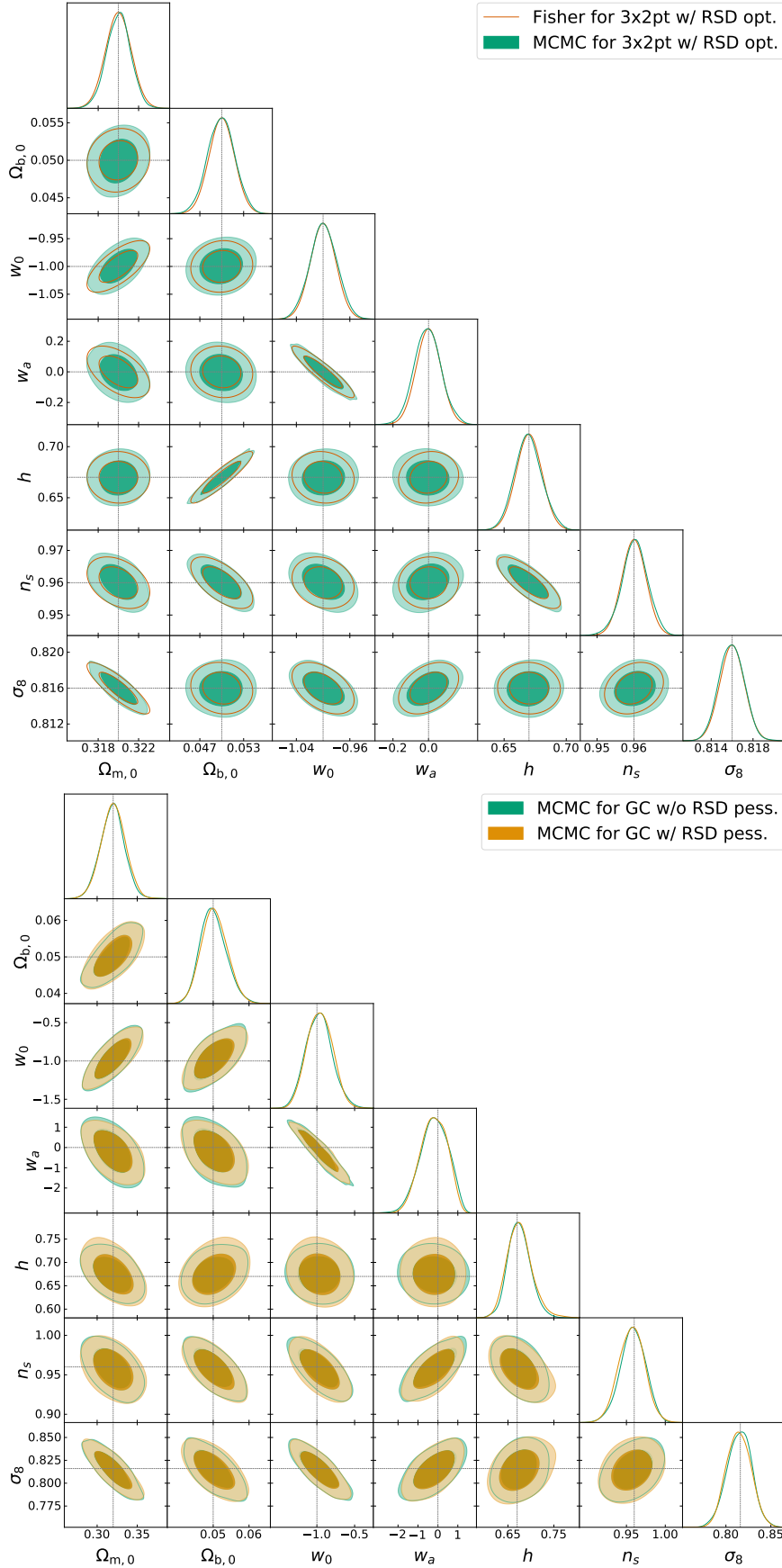
Fig. 4. The 68% and 95% C.L. marginalised contours along with the one-dimensional posterior distributions on the cosmological parameters. *Top:* Constraints from the 3×2pt analysis of the flat $w_0 w_a$CDM model for the optimistic scale cut considering RSD. The filled green contours are the MCMC constraints while the open orange ones are the Fisher ellipses for the same modelling. The fiducial cosmology model is marked with dotted, black lines. *Bottom:* Constraints from the GC alone of the flat $w_0 w_a$CDM model (pessimistic scenario), w/ (orange) and w/o (green) RSD. The fiducial cosmology model is marked with dotted, black lines.

Table 3. Summary of the mean estimated values, θ^*, along their corresponding 68% C.L. intervals, σ_θ, and the relative bias, B_θ (see Eq. 22) of a given parameter.

Parameter	Scale cut	w/ RSD			w/o RSD		
		θ^*	σ_θ	B_θ	θ^*	σ_θ	B_θ
$\Omega_{m,0}$	pess.	0.3193	0.0052	0.134	0.3019	0.0044	**4.11**
	opt.	0.3197	0.0037	0.08	0.3022	0.0033	**5.39**
$\Omega_{b,0}$	pess.	0.0503	0.0024	0.125	0.0499	0.0022	0.045
	opt.	0.0502	0.0018	0.111	0.0506	0.0018	0.33
h	pess.	0.674	0.023	0.174	0.668	0.021	0.095
	opt.	0.672	0.015	0.133	0.673	0.016	0.18
σ_8	pess.	0.8154	0.0059	0.101	0.8327	0.0062	**2.69**
	opt.	0.816	0.0013	0.0	0.8206	0.0013	**3.53**
n_s	pess.	0.96	0.012	0.0	0.959	0.011	0.091
	opt.	0.9596	0.0037	0.108	0.9684	0.0038	**2.21**
S_8	pess.	0.8412	0.0095	0.164	0.8353	0.009	0.829
	opt.	0.8424	0.0046	0.078	0.8236	0.0043	**4.45**

Note: These are the results of the GC analysis for each ΛCDM cosmological parameter for the complete (w/ RSD) and the incomplete (w/o RSD) model and for the pessimistic and optimistic scale cuts. We highlight the most biased cases ($B_\theta > 1$) with **bold**.

Table 4. Same as Table 3 for GC but for the $w_0 w_a$CDM model.

Parameter	Scale cut	w/ RSD			w/o RSD		
		θ^*	σ_θ	B_θ	θ^*	σ_θ	B_θ
$\Omega_{m,0}$	opt.	0.3190	0.0069	0.145	0.3092	0.0056	**1.928**
$\Omega_{b,0}$	opt.	0.0499	0.0019	0.052	0.0516	0.0019	0.84
h	opt.	0.672	0.018	0.11	0.664	0.016	0.37
σ_8	opt.	0.8166	0.003	0.2	0.8158	0.0027	0.074
n_s	opt.	0.96	0.0043	0.0	0.9669	0.0043	**1.60**
w_0	opt.	−1.001	0.042	0.0238	−1.007	0.039	0.17
w_a	opt.	−0.02	0.18	0.111	0.21	0.17	**1.235**
S_8	opt.	0.842	0.007	0.108	0.8281	0.0058	**2.52**

the input fiducial value (our benchmark) given the expected uncertainty on the parameter. Massey et al. (2012) suggests that, after taking into account systematic effects, values of $B_\theta \gtrsim 0.3$ can be considered already as statistically significant [6].

All the ΛCDM results in GC for the correct and incorrect model, as well as the pessimistic and optimistic scale cuts, are shown in Table 3. We opt to present in the top panel of Fig. 5 the incorrect model constraints for the optimistic cases alone since the resulting biases are larger than those in the pessimistic cut. We notice that, in the pessimistic case, neglecting RSD leads to a bias of 4.11 and 2.69 on parameters $\Omega_{m,0}$ and σ_8, respectively; while with the correct modelling we always recover the fiducial cosmology with $B_\theta \lesssim 0.3$ (see again Table 3). This bias is also imprinted on the increase of the best-fit value by $\Delta\chi^2 \approx 84.61$ with respect to the correct model.

The picture is similar for the optimistic scale cut, as we can see in the green contours of the top panel of Fig. 5. Here, we note that the bias on the same parameters increases, and another mild tension now arises on n_s. In particular, parameters $\Omega_{m,0}$, σ_8, and n_s are biased with values 5.39, 3.53, and 2.21, respectively, and as expected there is increase of $\Delta\chi^2 \approx 92.48$ with respect to the correct model. This bias increase in the optimistic scenario compared to the pessimistic can be explained as follows: by extending the range to higher multipoles, we do not include more signal from the linear RSD which, as we saw in Sect. 2.2, contributes only on large scales ($\ell \lesssim 100$). On the other hand, we increase

the constraining power on the parameters, meaning that any existing tension is enhanced by lowering the projected errors, a fact that shows that an inaccurate modelling becomes progressively more crucial, the more the quality of data improves.

We turn now our attention to the results obtained assuming the $w_0 w_a$CDM model. Again, we only consider the optimistic scales cut. The reason for this is that GC alone for the pessimistic scale cut is not very constraining in this model, and the bias on the parameters is expected to be small due to the smaller range of scales and the larger parameter set. The result of all this is that w_0 and w_a parameters vary over a large range in the MCMC, also in regions where $w_0 + w_a$ can take non-negative values (see Cepa, J. 2004, for details on the high-redshift limit of $w(z)$ in CPL). In such a region of the parameter space, CAMB cannot obtain meaningful cosmological quantities, and these points are automatically rejected from the chain, thus introducing a cut in the parameter space which is physically motivated. Based on this restriction along with the fact that the modelling for this case is not very constraining irrespective of the assumed prior on the CPL parameters, we decided to focus our analysis only to the optimistic case. The results are shown in Table 4 and the top panel of Fig. 5, where we still have biased estimates of our free parameters, although with reduced significance with respect to the ΛCDM analysis, due to the increased uncertainty brought by keeping the dark energy parameters w_0 and w_a free; we find that the parameters shifted by more than 1σ are $\Omega_{m,0}$, n_s, and w_a, with their B_θ values being 1.9, 1.6, and 1.2, respectively. Again, there is an increase of $\Delta\chi^2 \approx 90.65$ compared to the complete model. We summarise all the B_θ values for the aforementioned scenar-

---

[6] Values of $B_\theta < 0.3$ are considered to be permissible within the statistical fluctuation assuming that the same information for the synthetic data and the theory modelling has been used.
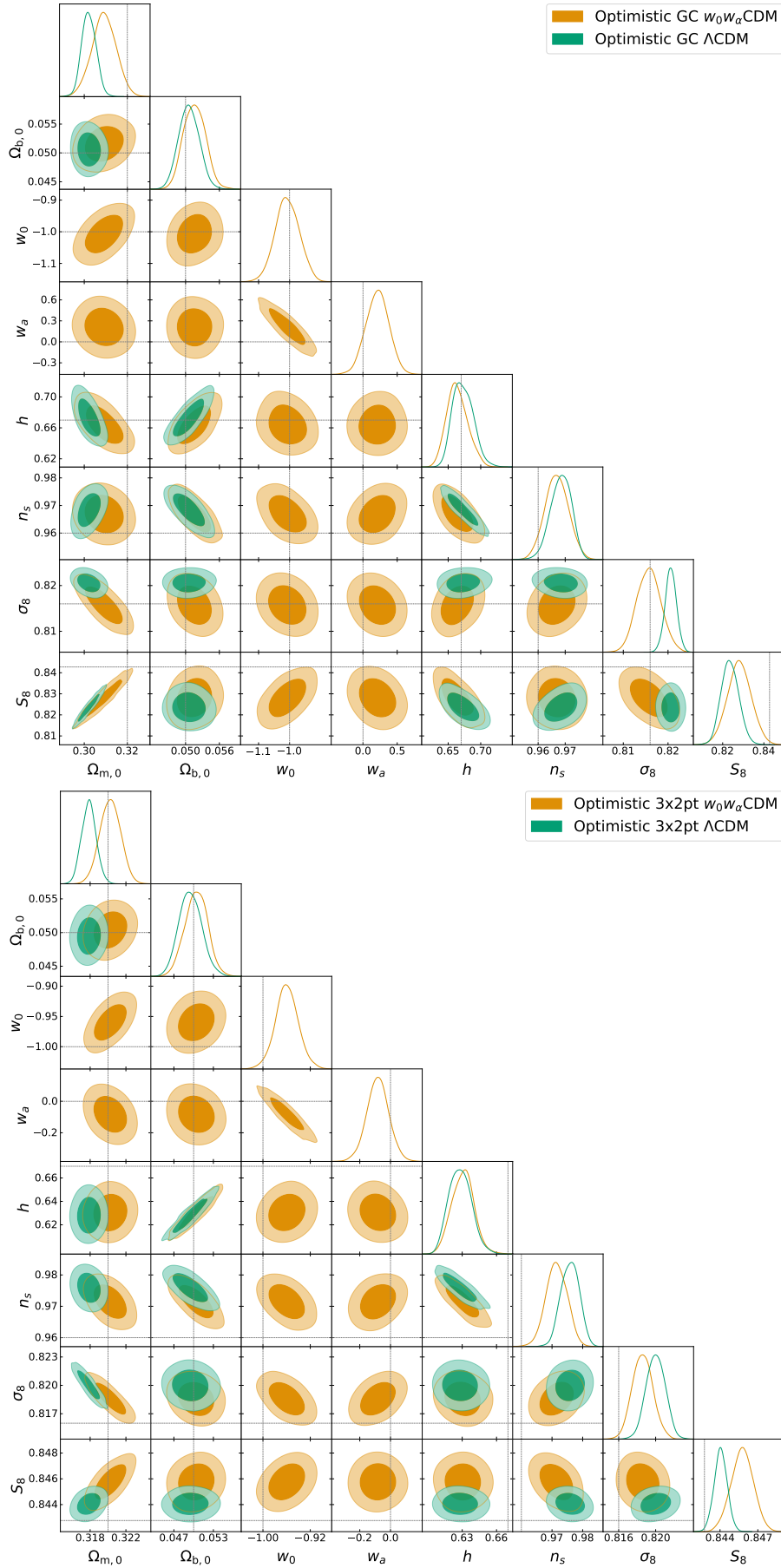
Fig. 5. The 68% and 95% C.L. marginalised contours alongside the corresponding one-dimensional posterior distributions of the cosmological parameters for the incorrect modelling (w/o RSD). *Top:* Constraints from the GC, of the ΛCDM (green contours) and w_0w_aCDM model (orange contours) for the optimistic scale cut. The fiducial cosmology is marked by dotted black lines. *Bottom:* Same as above, but for 3×2pt.

ios in the left panel of Fig. 6 (see caption for details), where we can easier appreciate the trend for larger biases in the optimistic cases compared to the pessimistic ones and those of the ΛCDM model against the w_0w_aCDM extension.

4.3.2. Biased parameter constraints in the 3×2pt

We repeat exactly the same analysis (different cosmologies and scale cuts) but now for the 3×2pt (Table 5, Table 6, and bottom panel of Fig. 5). Similarly to what we saw in Sect. 4.3.1 for the ΛCDM model and the pessimistic scale cuts, the parameters $\Omega_{m,0}$, h, n_s, and σ_8 are now biased by 3.52, 3.21, 2.05, and 3.96 (see Table 5), while the overall $\Delta\chi^2$ compared to the correct model is increased by 96.27. It is interesting to notice that, while some of the parameters (like n_s and h) exhibit an increased B_θ value due to the increased constraining power of the 3×2pt combination, for the other parameters the behaviour is less straightforward. On the one hand, WL strongly constrains S_8 – a combination of $\Omega_{m,0}$ and σ_8 – and, as this probe is not biased by neglecting RSD, one would expect these parameters to have their bias reduced. On the other hand, however, the inclusion of XC lifts the degeneracy between σ_8 and the bias parameters present in the GC probe, thus making the latter more sensitive to this parameter. Since both GC and XC are biased when we neglect RSD, the overall effect is an increased B_θ value on σ_8 with respect to the GC alone case.

In the optimistic case, the balance between these effects changes, as the increased amount of scales available for WL makes this more relevant, thus reducing the bias with respect to the GC alone case. This does not apply to n_s and h, which are still mostly constrained by GC. The $\Delta\chi^2$ is increased by 106.78 with respect to the correct model.

Finally, the results of the 3×2pt and the w_0w_aCDM model are shown in Table 6. In the pessimistic case, we notice a biased estimate for σ_8 at 2.54, and misplaced peaks for the parameters $\Omega_{m,0}$, $\Omega_{b,0}$, w_0, and h with biases 1.17, 0.83, 1.25, and 1.00, while for the optimistic scenario (see again Table 6 and the orange contours of the bottom panel of Fig. 5), there are biased estimates for w_0, w_a, h, n_s, and σ_8 at 2.00, 1.14, 4.02, 3.28, and 2.36, respectively. Both models yield an increased $\Delta\chi^2$ compared to the complete model by 92.05 (pessimistic) and 103.6 (optimistic). When comparing the latter case to GC alone, we can notice how the increased constraining power, brought by WL and XC, has the effect of increasing the significance of the bias on most of the parameters. Similarly to Sect. 4.3.1, we summarise the B_θ values for all the cases of the 3×2pt in the right panel of Fig. 6.

5. Conclusions

In this work, we have aimed to quantify the contribution of linear redshift-space distortions (RSD) in photometric galaxy clustering (GC) as expected to be measured by *Euclid*, both as a stand-alone probe and in combination with cosmic shear (WL), in the so-called 3×2pt approach. We followed Tanidis & Camera (2019) to include RSD in the angular power spectra of GC and of its cross-correlation with WL (XC).

Using the galaxy distribution information coming from the Flagship simulation, and the *Euclid* specifications discussed in EP:VII, we generated synthetic data by generating angular power spectra and covariance matrix with a fiducial cosmology, for the photometric observations of *Euclid* and produced the posterior distributions for the free parameters of our model in a Markov chain Monte Carlo framework.

As a first step, we validated our results against a Fisher matrix approach finding a very good agreement. Then, we compared the constraints on cosmological parameters obtained when the theoretical predictions are computed including the contribution of RSD to those obtained when RSD are neglected. We find that using GC as a stand-alone probe, and assuming a ΛCDM cosmology for the theoretical predictions, neglecting RSD can lead to significant inaccuracies on the reconstruction of cosmological parameters – in particular in the most optimistic case where the constraining power of our experimental setup is maximum. We find that parameters $\Omega_{m,0}$, n_s, and σ_8 are all significantly shifted from their (input) fiducial values, respectively with biases of $5.4\,\sigma$, $2.2\,\sigma$, and $3.5\,\sigma$. The statistical significance of these shifts is however reduced when the cosmological model used to fit the data allows for w_0 and w_a parameters to take values different from ΛCDM. The inclusion of these two extra parameters degrades the constraining power and leads to a less evident shift with respect to the fiducial model.

At this point, we included WL and XC in the analysis, performing a 3×2pt analysis. In this case, we found a non-trivial effect on the significance of the RSD contribution. On the one hand, WL contributes to tighten the constraints achievable with *Euclid*, thus potentially increasing the significance of the shifts one obtains when neglecting RSD. On the other hand, theoretical predictions for this probe are not biased by such an approximation (although the XC is still biased), and the inclusion of WL can therefore drag the recovered posterior distribution towards the fiducial values even when RSD are neglected. Indeed, we found that for parameters like n_s and h, where galaxy GC dominate, WL simply improve the constraining power, and the bias on these parameters increases in significance. On the contrary, when looking at the parameters mostly constrained by WL, such as $\Omega_{m,0}$ and σ_8, we found that their shifts decrease in the optimistic case, where the constraining power of WL dominates the one from GC.

Summarising, we found that not including the contribution of linear RSD in the theoretical predictions for GC angular power spectra can significantly reduce the accuracy but not the precision of the constraints that can be achieved by *Euclid*. This happens due to the fact that the linear RSD contribute at scales $\ell < 100$, a cosmic-variance dominated regime yielding no gain in cosmological information. It is important to note that the necessity to include the effect of linear RSD in GC in order to avoid cosmology biases has been studied in depth in the literature (Scharf et al. 1994; Heavens & Taylor 1995; Padmanabhan et al. 2007; Blake et al. 2007; Nock et al. 2010; Crocce et al. 2011; Balaguera-Antolínez et al. 2018; Abbott et al. 2022) and the findings of our work agree with this. However, here, we have demonstrated that the approach of Tanidis & Camera (2019), which is a fast and approximated way to account for the linear RSD correction, can be easily implemented and tested within a parameter estimation pipeline in the modelling of *Euclid* photometric observables. In addition to this, there is an ongoing work to improve the modelling and study the effect of the non-linear galaxy bias in the photometric GC, which becomes especially important for Stage-IV galaxy surveys like *Euclid*.

Table 5. Same as Table 3 but for the 3×2pt.

Parameter	scale cut	w/ RSD			w/o RSD		
		θ^*	σ_θ	B_θ	θ^*	σ_θ	B_θ
$\Omega_{m,0}$	pess.	0.32	0.0025	0.0	0.3119	0.0023	**3.52**
	opt.	0.32006	0.00082	0.07317	0.31786	0.00082	**2.61**
$\Omega_{b,0}$	pess.	0.05	0.0022	0.0	0.0481	0.002	0.95
	opt.	0.0501	0.0018	0.0555	0.0495	0.0017	0.29
h	pess.	0.671	0.016	0.062	0.625	0.014	**3.21**
	opt.	0.671	0.011	0.090	0.6283	0.01015	**4.11**
σ_8	pess.	0.816	0.0032	0.0	0.8279	0.003	**3.96**
	opt.	0.816	0.001	0.0	0.82	0.001	**4.0**
n_s	pess.	0.9596	0.0078	0.0512	0.9747	0.0072	**2.05**
	opt.	0.9598	0.0031	0.0645	0.9759	0.003	**5.3**
S_8	pess.	0.8428	0.00073	0.0531	0.84422	0.00072	**2.026**
	opt.	0.8428	0.00054	0.07189	0.84405	0.00052	**2.478**

Table 6. Same as Table 4 but for the 3×2pt.

Parameter	scale cut	w/ RSD			w/o RSD		
		θ^*	σ_θ	B_θ	θ^*	σ_θ	B_θ
$\Omega_{m,0}$	pess.	0.3202	0.0038	0.0526	0.3159	0.0035	**1.17**
	opt.	0.32	0.0012	0.0	0.3202	0.0012	0.16
$\Omega_{b,0}$	pess.	0.0502	0.0025	0.0799	0.0520	0.0024	0.83
	opt.	0.0499	0.0019	0.0526	0.0504	0.0017	0.23
h	pess.	0.671	0.019	0.0526	0.653	0.017	1.0
	opt.	0.67	0.01	0.0	0.6306	0.0098	**4.02**
σ_8	pess.	0.8158	0.0047	0.0425	0.8272	0.0044	**2.54**
	opt.	0.816	0.0012	0.0	0.8186	0.0011	**2.36**
n_s	pess.	0.9595	0.0094	0.0531	0.9557	0.0087	0.49
	opt.	0.9602	0.0035	0.0571	0.9715	0.0035	**3.28**
w_0	pess.	−0.9996	0.046	0.0086	−0.945	0.044	1.25
	opt.	−0.999	0.02	0.05	−0.96	0.02	**2.0**
w_a	pess.	0.0	0.18	0.0	0.02	0.16	0.125
	opt.	−0.005	0.075	0.066	−0.083	0.073	**1.136**
S_8	pess.	0.8428	0.0014	0.0277	0.8488	0.0014	**4.31**
	opt.	0.84273	0.00086	0.0362	0.84576	0.00089	**3.37**

References

Abbott, T. M. C., Abdalla, F. B., Annis, J., et al. 2018, MNRAS, 480, 3879

Abbott, T. M. C., Aguena, M., Alarcon, A., et al. 2022, Phys. Rev. D, 105, 023520

Abdalla, F. B., Bull, P., Camera, S., et al. 2015, in Advancing Astrophysics with the Square Kilometre Array (AASKA14), 17

Alsing, J., Kirk, D., Heavens, A., & Jaffe, A. H. 2015, MNRAS, 452, 1202

Amendola, L., Appleby, S., Avgoustidis, A., et al. 2018, Living Rev. Rel., 21, 2

Amendola, L., Appleby, S., Bacon, D., et al. 2013, Living Rev. Rel., 16, 6

Andrade-Oliveira, F., Camacho, H., Faga, L., et al. 2021, MNRAS, 505, 5714

Balaguera-Antolínez, A., Bilicki, M., & Branchini, E. 2018, MNRAS., 476, 1050

Behroozi, P. S., Wechsler, R. H., & Wu, H.-Y. 2013, ApJ, 762, 109

Bird, S., Viel, M., & Haehnelt, M. G. 2012, MNRAS, 420, 2551

Blake, C., Collister, A., & Bridle, S. 2007, MRAS, 374, 1527

Blanton, M. R., Hogg, D. W., Bahcall, N. A., et al. 2003, ApJ, 594, 186

Blanton, M. R., Lupton, R. H., Schlegel, D. J., et al. 2005, ApJ, 631, 208

Blanton, M. R., Schlegel, D. J., Strauss, M. A., et al. 2005, AJ, 129, 2562

Bonvin, C. & Durrer, R. 2011, Phys. Rev., D84, 063505

Brown, M., Bacon, D., Camera, S., et al. 2015, in Advancing Astrophysics with the Square Kilometre Array (AASKA14), 23

Bull, P., Camera, S., Raccanelli, A., et al. 2015, in Advancing Astrophysics with the Square Kilometre Array (AASKA14), 24

Camera, S., Maartens, R., & Santos, M. G. 2015a, MNRAS, 451, L80

Camera, S., Raccanelli, A., Bull, P., et al. 2015b, in Advancing Astrophysics with the Square Kilometre Array (AASKA14), 25

Carretero, J., Castander, F. J., Gaztañaga, E., Crocce, M., & Fosalba, P. 2015, MNRAS, 447, 646

Cepa, J. 2004, A&A, 422, 831

Challinor, A. & Lewis, A. 2011, Phys. Rev., D84, 043516

Chevallier & Polarski. 2001, International Journal of Modern Physics D, 10, 213

Costille, A., Caillat, A., Rossin, C., et al. 2018, in Space Telescopes and Instrumentation 2018: Optical, Infrared, and Millimeter Wave, ed. M. Lystrup, H. A. MacEwen, G. G. Fazio, N. Batalha, N. Siegler, & E. C. Tong, Vol. 10698, International Society for Optics and Photonics (SPIE), 730

Crocce, M., Cabré, A., & Gaztañaga, E. 2011, MNRAS, 414, 329

Cropper, M., Pottinger, S., Azzollini, R., et al. 2018, in Space Telescopes and Instrumentation 2018: Optical, Infrared, and Millimeter Wave, ed. M. Lystrup, H. A. MacEwen, G. G. Fazio, N. Batalha, N. Siegler, & E. C. Tong, Vol. 10698, International Society for Optics and Photonics (SPIE), 709

De Vicente, J., Sánchez, E., & Sevilla-Noarbe, I. 2016, MNRAS, 459, 3078

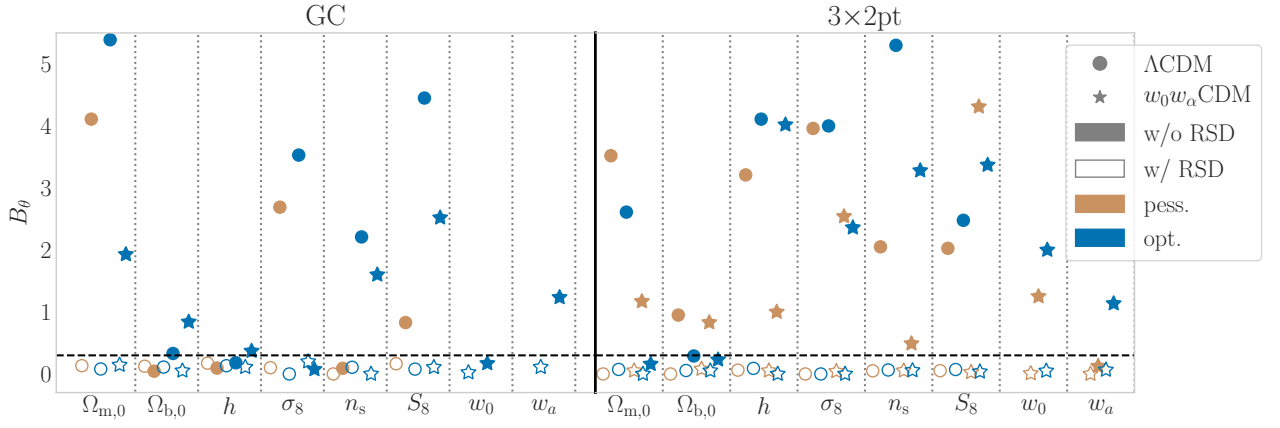DES Collaboration: Abbott, T., Aldering, G., Annis, J., et al. 2005 [arXiv:astro-ph/0510346]

Fig. 6. Summary plot of the B_θ values for the GC (left) and the 3×2pt (right) for all the examined cases. The circles correspond to the ΛCDM cosmology model and the stars to the $w_0 w_\alpha$CDM extension, while open and filled symbols to a theory modelling w/ and w/o RSD, respectively. Pessimistic and optimistic scale cuts are shown with brown and blue color. The horizontal dashed line denotes the value $B_\theta = 0.3$

DESI Collaboration: Aghamousa, A., Aguilar, J., Ahlen, S., et al. 2016a [arXiv:1611.00036]
DESI Collaboration: Aghamousa, A., Aguilar, J., Ahlen, S., et al. 2016b [arXiv:1611.00037]
Desjacques, V., Jeong, D., & Schmidt, F. 2018, Physics Reports, 733, 1
Doré, O., Bock, J., Ashby, M., et al. 2014 [arXiv:1412.4872]
Doré, O., Werner, M. W., Ashby, M. L. N., et al. 2018 [arXiv:1805.05489]
Elvin-Poole, J., Crocce, M., Ross, A. J., et al. 2018, Phys. Rev., D98, 042006
Euclid Collaboration: Ajani, V., Baldi, M., Barthelemy, A., et al. 2023, A&A, 675, A120
Euclid Collaboration: Blanchard, A., Camera, S., Carbone, C., et al. 2020, A&A, 642, A191
Euclid Collaboration: Pocino, A., Tutusaus, I., Castander, F. J., et al. 2021, A&A, 655, A44
Foreman-Mackey, D., Hogg, D. W., Lang, D., & Goodman, J. 2013, Publ. Astron. Soc. Pac., 125, 306
Heavens, A., Alsing, J., & Jaffe, A. H. 2013, MNRAS, 433, L6
Heavens, A. F. & Taylor, A. N. 1995, MNRAS, 275, 483
Howlett, C., Lewis, A., Hall, A., & Challinor, A. 2012, JCAP, 2012, 027
Ivezić, v., Kahn, S. M., Tyson, A. J., et al. 2019, ApJ, 873, 111
Joachimi, B., Cacciato, M., Kitching, T. D., et al. 2015, Space Science Reviews, 193, 1
Kaiser, N. 1987, MNRAS, 227, 1
Kaiser, N. 1992, ApJ, 388, 272
Laureijs, R., Amiaux, J. Arduini, S., et al. 2011 [arXiv:1110.3193]
Lepori, F., Tutusaus, I., Viglione, C., et al. 2022, A&A, 662, A93
Lewis, A., Challinor, A., & Lasenby, A. 2000, ApJ, 538, 473
Linder, E. V. 2003, Phys. Rev. Lett., 90, 091301
LSST Dark Energy Science Collaboration: Mandelbaum, R., Eifler, T., Hložek, R., et al. 2018 [arXiv:1809.01669]
LSST Science Collaboration: Abell, P., A., Allison, J., Anderson, S., F., et al. 2009 [arXiv:0912.0201]
Martinelli, M., Dalal, R., Majidi, F., et al. 2022, MNRAS, 510, 1964
Massey, R., Hoekstra, H., Kitching, T., et al. 2012, MNRAS, 429, 661
Nock, K., Percival, W. J., & Ross, A. J. 2010, MNRAS, 407, 520
Padmanabhan, N., Schlegel, D. J., Seljak, U., et al. 2007, MNRAS, 378, 852
Potter, D., Stadel, J., & Teyssier, R. 2017, Computational Astrophysics and Cosmology, 4, 2
Raccanelli, A., Bull, P., Camera, S., et al. 2015, in Advancing Astrophysics with the Square Kilometre Array (AASKA14), 31
Santos, M., Bull, P., Alonso, D., et al. 2015, in Advancing Astrophysics with the Square Kilometre Array (AASKA14), 19
Scharf, C. A., Fisher, K. B., & Lahav, O. 1994, MRAS, 266, 219
Schneider, P., Eifler, T., & Krause, E. 2010, A&A, 520, A116
SKA Cosmology Science Working Group. 2020, PASA, 37, e007
Smith, R. E., Peacock, J. A., Jenkins, A., et al. 2003, MNRAS, 341, 1311
Spergel, D., Gehrels, N., Baltay, C., et al. 2015 [arXiv:1503.03757]
Szalay, A. S., Matsubara, T., & Landy, S. D. 1998, ApJ, 498, L1
Sánchez, A. G., Scoccimarro, R., Crocce, M., et al. 2016, MNRAS, 464, 1640
Takahashi, R., Sato, M., Nishimichi, T., Taruya, A., & Oguri, M. 2012, ApJ, 761, 152
Tanidis, K. & Camera, S. 2019, MNRAS, 489, 3385
Tanidis, K., Camera, S., & Parkinson, D. 2019, MNRAS, 491, 4869
Yoo, J. 2010, Phys. Rev., D82, 083508

Zehavi, I., Zheng, Z., Weinberg, D. H., et al. 2011, ApJ, 736, 59
Zuntz, J., Paterno, M., Jennings, E., et al. 2015, Astron. Comput., 12, 45

[1] CEICO, Institute of Physics of the Czech Academy of Sciences, Na Slovance 2, Praha 8, Czech Republic
[2] Department of Physics, Oxford University, Keble Road, Oxford OX1 3RH, UK
[3] INAF-Osservatorio Astronomico di Roma, Via Frascati 33, 00078 Monteporzio Catone, Italy
[4] INFN-Sezione di Roma, Piazzale Aldo Moro, 2 - c/o Dipartimento di Fisica, Edificio G. Marconi, 00185 Roma, Italy
[5] Institut de Recherche en Astrophysique et Planétologie (IRAP), Université de Toulouse, CNRS, UPS, CNES, 14 Av. Edouard Belin, 31400 Toulouse, France
[6] Université de Genève, Département de Physique Théorique and Centre for Astroparticle Physics, 24 quai Ernest-Ansermet, CH-1211 Genève 4, Switzerland
[7] Dipartimento di Fisica, Universitá degli Studi di Torino, Via P. Giuria 1, 10125 Torino, Italy
[8] INFN-Sezione di Torino, Via P. Giuria 1, 10125 Torino, Italy
[9] INAF-Osservatorio Astrofisico di Torino, Via Osservatorio 20, 10025 Pino Torinese (TO), Italy
[10] Université Paris-Saclay, CNRS, Institut d'astrophysique spatiale, 91405, Orsay, France
[11] Institute of Cosmology and Gravitation, University of Portsmouth, Portsmouth PO1 3FX, UK
[12] INAF-Osservatorio Astronomico di Brera, Via Brera 28, 20122 Milano, Italy
[13] INAF-Osservatorio di Astrofisica e Scienza dello Spazio di Bologna, Via Piero Gobetti 93/3, 40129 Bologna, Italy
[14] Dipartimento di Fisica e Astronomia, Universitá di Bologna, Via Gobetti 93/2, 40129 Bologna, Italy
[15] INFN-Sezione di Bologna, Viale Berti Pichat 6/2, 40127 Bologna, Italy
[16] Dipartimento di Fisica, Universitá di Genova, Via Dodecaneso 33, 16146, Genova, Italy
[17] INFN-Sezione di Genova, Via Dodecaneso 33, 16146, Genova, Italy
[18] Department of Physics "E. Pancini", University Federico II, Via Cinthia 6, 80126, Napoli, Italy
[19] INAF-Osservatorio Astronomico di Capodimonte, Via Moiariello 16, 80131 Napoli, Italy
[20] Instituto de Astrofísica e Ciências do Espaço, Universidade do Porto, CAUP, Rua das Estrelas, PT4150-762 Porto, Portugal
[21] INAF-IASF Milano, Via Alfonso Corti 12, 20133 Milano, Italy
[22] Institut de Física d'Altes Energies (IFAE), The Barcelona Institute of Science and Technology, Campus UAB, 08193 Bellaterra (Barcelona),

Spain

[23] Port d'Informació Científica, Campus UAB, C. Albareda s/n, 08193 Bellaterra (Barcelona), Spain

[24] Institute for Theoretical Particle Physics and Cosmology (TTK), RWTH Aachen University, 52056 Aachen, Germany

[25] INFN section of Naples, Via Cinthia 6, 80126, Napoli, Italy

[26] Dipartimento di Fisica e Astronomia "Augusto Righi" - Alma Mater Studiorum Universitá di Bologna, Viale Berti Pichat 6/2, 40127 Bologna, Italy

[27] Centre National d'Etudes Spatiales – Centre spatial de Toulouse, 18 avenue Edouard Belin, 31401 Toulouse Cedex 9, France

[28] Institut national de physique nucléaire et de physique des particules, 3 rue Michel-Ange, 75794 Paris Cédex 16, France

[29] Institute for Astronomy, University of Edinburgh, Royal Observatory, Blackford Hill, Edinburgh EH9 3HJ, UK

[30] European Space Agency/ESRIN, Largo Galileo Galilei 1, 00044 Frascati, Roma, Italy

[31] ESAC/ESA, Camino Bajo del Castillo, s/n., Urb. Villafranca del Castillo, 28692 Villanueva de la Cañada, Madrid, Spain

[32] University of Lyon, Univ Claude Bernard Lyon 1, CNRS/IN2P3, IP2I Lyon, UMR 5822, 69622 Villeurbanne, France

[33] Institute of Physics, Laboratory of Astrophysics, Ecole Polytechnique Fédérale de Lausanne (EPFL), Observatoire de Sauverny, 1290 Versoix, Switzerland

[34] UCB Lyon 1, CNRS/IN2P3, IUF, IP2I Lyon, 4 rue Enrico Fermi, 69622 Villeurbanne, France

[35] Departamento de Física, Faculdade de Ciências, Universidade de Lisboa, Edifício C8, Campo Grande, PT1749-016 Lisboa, Portugal

[36] Instituto de Astrofísica e Ciências do Espaço, Faculdade de Ciências, Universidade de Lisboa, Campo Grande, 1749-016 Lisboa, Portugal

[37] Department of Astronomy, University of Geneva, ch. d'Ecogia 16, 1290 Versoix, Switzerland

[38] INFN-Padova, Via Marzolo 8, 35131 Padova, Italy

[39] INAF-Istituto di Astrofisica e Planetologia Spaziali, via del Fosso del Cavaliere, 100, 00100 Roma, Italy

[40] Université Paris-Saclay, Université Paris Cité, CEA, CNRS, AIM, 91191, Gif-sur-Yvette, France

[41] Institute of Space Sciences (ICE, CSIC), Campus UAB, Carrer de Can Magrans, s/n, 08193 Barcelona, Spain

[42] Institut d'Estudis Espacials de Catalunya (IEEC), Carrer Gran Capitá 2-4, 08034 Barcelona, Spain

[43] INAF-Osservatorio Astronomico di Trieste, Via G. B. Tiepolo 11, 34143 Trieste, Italy

[44] Aix-Marseille Université, CNRS/IN2P3, CPPM, Marseille, France

[45] INAF-Osservatorio Astronomico di Padova, Via dell'Osservatorio 5, 35122 Padova, Italy

[46] Max Planck Institute for Extraterrestrial Physics, Giessenbachstr. 1, 85748 Garching, Germany

[47] University Observatory, Faculty of Physics, Ludwig-Maximilians-Universität, Scheinerstr. 1, 81679 Munich, Germany

[48] Dipartimento di Fisica "Aldo Pontremoli", Universitá degli Studi di Milano, Via Celoria 16, 20133 Milano, Italy

[49] INFN-Sezione di Milano, Via Celoria 16, 20133 Milano, Italy

[50] Institute of Theoretical Astrophysics, University of Oslo, P.O. Box 1029 Blindern, 0315 Oslo, Norway

[51] Jet Propulsion Laboratory, California Institute of Technology, 4800 Oak Grove Drive, Pasadena, CA, 91109, USA

[52] Department of Physics, Lancaster University, Lancaster, LA1 4YB, UK

[53] Technical University of Denmark, Elektrovej 327, 2800 Kgs. Lyngby, Denmark

[54] Cosmic Dawn Center (DAWN), Denmark

[55] Max-Planck-Institut für Astronomie, Königstuhl 17, 69117 Heidelberg, Germany

[56] Department of Physics and Astronomy, University College London, Gower Street, London WC1E 6BT, UK

[57] Department of Physics and Helsinki Institute of Physics, Gustaf Hällströmin katu 2, 00014 University of Helsinki, Finland

[58] Department of Physics, P.O. Box 64, 00014 University of Helsinki, Finland

[59] Helsinki Institute of Physics, Gustaf Hällströmin katu 2, University of Helsinki, Helsinki, Finland

[60] NOVA optical infrared instrumentation group at ASTRON, Oude Hoogeveensedijk 4, 7991PD, Dwingeloo, The Netherlands

[61] Universität Bonn, Argelander-Institut für Astronomie, Auf dem Hügel 71, 53121 Bonn, Germany

[62] Aix-Marseille Université, CNRS, CNES, LAM, Marseille, France

[63] Dipartimento di Fisica e Astronomia "Augusto Righi" - Alma Mater Studiorum Universitá di Bologna, via Piero Gobetti 93/2, 40129 Bologna, Italy

[64] Department of Physics, Institute for Computational Cosmology, Durham University, South Road, DH1 3LE, UK

[65] Université Côte d'Azur, Observatoire de la Côte d'Azur, CNRS, Laboratoire Lagrange, Bd de l'Observatoire, CS 34229, 06304 Nice cedex 4, France

[66] Université Paris Cité, CNRS, Astroparticule et Cosmologie, 75013 Paris, France

[67] European Space Agency/ESTEC, Keplerlaan 1, 2201 AZ Noordwijk, The Netherlands

[68] Department of Physics and Astronomy, University of Aarhus, Ny Munkegade 120, DK-8000 Aarhus C, Denmark

[69] Centre for Astrophysics, University of Waterloo, Waterloo, Ontario N2L 3G1, Canada

[70] Department of Physics and Astronomy, University of Waterloo, Waterloo, Ontario N2L 3G1, Canada

[71] Perimeter Institute for Theoretical Physics, Waterloo, Ontario N2L 2Y5, Canada

[72] Université Paris-Saclay, Université Paris Cité, CEA, CNRS, Astrophysique, Instrumentation et Modélisation Paris-Saclay, 91191 Gif-sur-Yvette, France

[73] Space Science Data Center, Italian Space Agency, via del Politecnico snc, 00133 Roma, Italy

[74] CEA Saclay, DFR/IRFU, Service d'Astrophysique, Bat. 709, 91191 Gif-sur-Yvette, France

[75] Institute of Space Science, Str. Atomistilor, nr. 409 Măgurele, Ilfov, 077125, Romania

[76] Dipartimento di Fisica e Astronomia "G. Galilei", Universitá di Padova, Via Marzolo 8, 35131 Padova, Italy

[77] Universitäts-Sternwarte München, Fakultät für Physik, Ludwig-Maximilians-Universität München, Scheinerstrasse 1, 81679 München, Germany

[78] Departamento de Física, FCFM, Universidad de Chile, Blanco Encalada 2008, Santiago, Chile

[79] Satlantis, University Science Park, Sede Bld 48940, Leioa-Bilbao, Spain

[80] Centro de Investigaciones Energéticas, Medioambientales y Tecnológicas (CIEMAT), Avenida Complutense 40, 28040 Madrid, Spain

[81] Instituto de Astrofísica e Ciências do Espaço, Faculdade de Ciências, Universidade de Lisboa, Tapada da Ajuda, 1349-018 Lisboa, Portugal

[82] Universidad Politécnica de Cartagena, Departamento de Electrónica y Tecnología de Computadoras, Plaza del Hospital 1, 30202 Cartagena, Spain

[83] Kapteyn Astronomical Institute, University of Groningen, PO Box 800, 9700 AV Groningen, The Netherlands

[84] INFN-Bologna, Via Irnerio 46, 40126 Bologna, Italy

[85] Infrared Processing and Analysis Center, California Institute of Technology, Pasadena, CA 91125, USA

[86] IFPU, Institute for Fundamental Physics of the Universe, via Beirut 2, 34151 Trieste, Italy

[87] Instituto de Astrofísica de Canarias, Calle Vía Láctea s/n, 38204, San Cristóbal de La Laguna, Tenerife, Spain

[88] University of Applied Sciences and Arts of Northwestern Switzerland, School of Engineering, 5210 Windisch, Switzerland

[89] Institut d'Astrophysique de Paris, 98bis Boulevard Arago, 75014, Paris, France

[90] Junia, EPA department, 41 Bd Vauban, 59800 Lille, France

[91] Instituto de Física Teórica UAM-CSIC, Campus de Cantoblanco, 28049 Madrid, Spain

[92] CERCA/ISO, Department of Physics, Case Western Reserve University, 10900 Euclid Avenue, Cleveland, OH 44106, USA

[93] Laboratoire de Physique de l'École Normale Supérieure, ENS, Université PSL, CNRS, Sorbonne Université, 75005 Paris, France

[94] Observatoire de Paris, Université PSL, Sorbonne Université, LERMA, 750 Paris, France

[95] Astrophysics Group, Blackett Laboratory, Imperial College London, London SW7 2AZ, UK

[96] Scuola Normale Superiore, Piazza dei Cavalieri 7, 56126 Pisa, Italy

[97] SISSA, International School for Advanced Studies, Via Bonomea 265, 34136 Trieste TS, Italy

[98] INFN, Sezione di Trieste, Via Valerio 2, 34127 Trieste TS, Italy

[99] Departamento de Astrofísica, Universidad de La Laguna, 38206, La Laguna, Tenerife, Spain

[100] Dipartimento di Fisica e Scienze della Terra, Universitá degli Studi di Ferrara, Via Giuseppe Saragat 1, 44122 Ferrara, Italy

[101] Istituto Nazionale di Fisica Nucleare, Sezione di Ferrara, Via Giuseppe Saragat 1, 44122 Ferrara, Italy

[102] Institut de Physique Théorique, CEA, CNRS, Université Paris-Saclay 91191 Gif-sur-Yvette Cedex, France

[103] Institut d'Astrophysique de Paris, UMR 7095, CNRS, and Sorbonne Université, 98 bis boulevard Arago, 75014 Paris, France

[104] Dipartimento di Fisica - Sezione di Astronomia, Universitá di Trieste, Via Tiepolo 11, 34131 Trieste, Italy

[105] NASA Ames Research Center, Moffett Field, CA 94035, USA

[106] Kavli Institute for Particle Astrophysics & Cosmology (KIPAC), Stanford University, Stanford, CA 94305, USA

[107] INAF, Istituto di Radioastronomia, Via Piero Gobetti 101, 40129 Bologna, Italy

[108] Institute Lorentz, Leiden University, PO Box 9506, Leiden 2300 RA, The Netherlands

[109] Institute for Astronomy, University of Hawaii, 2680 Woodlawn Drive, Honolulu, HI 96822, USA

[110] Department of Physics & Astronomy, University of California Irvine, Irvine CA 92697, USA

[111] Departamento Física Aplicada, Universidad Politécnica de Cartagena, Campus Muralla del Mar, 30202 Cartagena, Murcia, Spain

[112] Department of Astronomy & Physics and Institute for Computational Astrophysics, Saint Mary's University, 923 Robie Street, Halifax, Nova Scotia, B3H 3C3, Canada

[113] Dipartimento di Fisica, Universitá degli studi di Genova, and INFN-Sezione di Genova, via Dodecaneso 33, 16146, Genova, Italy

[114] Department of Computer Science, Aalto University, PO Box 15400, Espoo, FI-00 076, Finland

[115] Ruhr University Bochum, Faculty of Physics and Astronomy, Astronomical Institute (AIRUB), German Centre for Cosmological Lensing (GCCL), 44780 Bochum, Germany

[116] Université Paris-Saclay, CNRS/IN2P3, IJCLab, 91405 Orsay, France

[117] Department of Physics and Astronomy, Vesilinnantie 5, 20014 University of Turku, Finland

[118] Serco for European Space Agency (ESA), Camino bajo del Castillo, s/n, Urbanizacion Villafranca del Castillo, Villanueva de la Cañada, 28692 Madrid, Spain

[119] AIM, CEA, CNRS, Université Paris-Saclay, Université de Paris, 91191 Gif-sur-Yvette, France

[120] Oskar Klein Centre for Cosmoparticle Physics, Department of Physics, Stockholm University, Stockholm, SE-106 91, Sweden

[121] Univ. Grenoble Alpes, CNRS, Grenoble INP, LPSC-IN2P3, 53, Avenue des Martyrs, 38000, Grenoble, France

[122] Centre de Calcul de l'IN2P3/CNRS, 21 avenue Pierre de Coubertin 69627 Villeurbanne Cedex, France

[123] Dipartimento di Fisica, Sapienza Università di Roma, Piazzale Aldo Moro 2, 00185 Roma, Italy

[124] Centro de Astrofísica da Universidade do Porto, Rua das Estrelas, 4150-762 Porto, Portugal

[125] Dipartimento di Fisica, Università di Roma Tor Vergata, Via della Ricerca Scientifica 1, Roma, Italy

[126] INFN, Sezione di Roma 2, Via della Ricerca Scientifica 1, Roma, Italy

[127] Department of Mathematics and Physics E. De Giorgi, University of Salento, Via per Arnesano, CP-I93, 73100, Lecce, Italy

[128] INAF-Sezione di Lecce, c/o Dipartimento Matematica e Fisica, Via per Arnesano, 73100, Lecce, Italy

[129] INFN, Sezione di Lecce, Via per Arnesano, CP-193, 73100, Lecce, Italy

[130] Institute for Computational Science, University of Zurich, Winterthurerstrasse 190, 8057 Zurich, Switzerland

[131] Institut für Theoretische Physik, University of Heidelberg, Philosophenweg 16, 69120 Heidelberg, Germany

[132] Université St Joseph; Faculty of Sciences, Beirut, Lebanon

[133] Mullard Space Science Laboratory, University College London, Holmbury St Mary, Dorking, Surrey RH5 6NT, UK

[134] Department of Astrophysical Sciences, Peyton Hall, Princeton University, Princeton, NJ 08544, USA

[135] Niels Bohr Institute, University of Copenhagen, Jagtvej 128, 2200 Copenhagen, Denmark

[136] Cosmic Dawn Center (DAWN)

[137] Universität Innsbruck, Institut für Astro- und Teilchenphysik, Technikerstr. 25/8, 6020 Innsbruck, Austria